

Method for overcoming the finite space-bandwidth limitation of digital holograms in holography

BYUNG GYU CHAE

Holographic Contents Research Laboratory, Electronics and Telecommunications Research Institute, 218 Gajeong-ro, Yuseong-gu, Daejeon 34129, Republic of Korea
bgchae@etri.re.kr

Abstract:

A digital hologram has a finite space-bandwidth, which determines the spatial resolution and angular field of view of its reconstructed image. However, a higher space-bandwidth induces aliased replica patterns in the Fresnel diffraction. This study analyzes the spatial distribution of the angular spectrum in an undersampled hologram within the complex domain. The replica functions are identified as higher spatial frequency components of the original function, with the spatial frequency range extending continuously from the original function into the region of the replica functions. Simulations of optical imaging show results consistent with theoretical analysis, demonstrating that imaging performance beyond the space-bandwidth limitation of a digital hologram is achievable. Specifically, a method is proposed to address the challenge of limited viewing angles in holographic displays based on this interpretation. This approach provides an alternative solution to overcome the constraints imposed by the finite space-bandwidth of digital holograms.

© 2024 Optica Publishing Group

1. Introduction

The holographic image is reconstructed either numerically or optically from the digital hologram. A digital hologram has a finite space-bandwidth, which determines key imaging performance metrics such as the resolution limit and angular field of view [1, 2]. The space-bandwidth B_w of the Fresnel hologram sampled at Δ pixel interval with $N \times N$ pixels is represented as

$$B_w = \frac{N\Delta}{\lambda z}. \quad (1)$$

According to the Abbe diffraction theory, the resolution limit R_{lim} of the reconstructed image is given as the reciprocal of this value, $R_{\text{lim}} = \frac{\lambda z}{N\Delta} = \frac{\lambda}{2 \sin \theta}$ [3–6]. In optical reconstruction, the viewing angle is twice the angle value θ . The hologram aperture further constrains the ability to capture the spatial frequency components of the diffractive wave.

Aliased replica patterns are formed when the required bandwidth exceeds the bandwidth supported by the hologram's pixel [7–10]. Spatial frequency components higher than the Nyquist frequency are aliased, making them appear as lower frequency components of the original function. The spatial frequency f increases linearly along the spatial direction, and the aliased frequency f_a is determined by the relationship:

$$f_a = |f - mf_s|, \quad (2)$$

where f_s is the sampling frequency and m is an integer [11]. This property results in the formation of replica functions that are spatially distributed at regular periodic intervals. Figure 1 illustrates the aliasing phenomenon for a point-source hologram sampled at a lower sampling rate. The complex-valued hologram $h(x, y)$ for a point object $\delta(x, y)$ is expressed as the impulse response

function, $h(x, y) = \frac{e^{ikz}}{i\lambda z} \exp \left[\frac{i\pi}{\lambda z} (x^2 + y^2) \right]$. Using the modulated form of the Fourier-transformed function, the sampled hologram at an interval Δx along the x -axis is written as follows [12, 13]:

$$\sum_n h(n\Delta x) \delta(x - n\Delta x) = \frac{1}{\Delta x} \sum_n c_n h \left(x + \frac{\lambda z n}{\Delta x} \right). \quad (3)$$

For simplicity, a one-dimensional description is used hereafter. The replication pattern are formed at a reduced period of $\frac{\lambda z}{s\Delta x}$ when undersampled by a factor s of Δx . Continuous response functions are obtained through the inverse Fourier transform of modulated angular spectra. The angular spectra, within the range of the original function, are folded at intervals determined by the folding frequency.

Previously, it was reported that this type of hologram reconstructs a holographic image with a space-bandwidth that spans the entire aperture of the digital hologram, regardless of aliased fringes [13–15]. This suggests that the replica functions correspond to the high spatial-frequency components of the hologram field. However, the above description of aliasing makes it difficult to explain numerical and experimental results. The space-bandwidth remains confined to the original function due to replication, meaning that the diffraction performance is limited to its initial value. As a result, establishing a unified understanding in this field has proven challenging to date.

In this letter, an angular spectrum in the undersampled hologram with aliased replica fringes is investigated in the complex domain. Analysis in the complex plane shows that the spatial frequency increases linearly across the region of the replica functions. The replica functions exhibit a modulation pattern created by a modulating wave, which corresponds to multiples of the sampling frequency. The spatial frequency of the replica function is derived from the sum of the frequencies of the modulating signal and the original function. The replica function plays a role in the higher frequency components of original function, as well as additive replication. Numerical simulation of optical imaging reveals a consistency of this scheme, and especially, an approach to recover the smaller viewing angle in holographic display is proposed.

2. Angular spectrum distribution of undersampled hologram

The spatial frequency in the Fresnel hologram is represented as $\frac{x}{\lambda z}$ from the quadratic phase term, which depends linearly on the lateral spatial distance. The distribution of spatial frequency in the undersampled hologram of a point source is investigated, particularly in the complex plane. The complex-valued hologram, consisting of 256×256 pixels with a $8\text{-}\mu\text{m}$ pixel pitch, was synthesized using a point object placed at a distance of a half of z_c , resulting in the formation of four replica Fresnel zones, as shown in Fig 1(a). A unit-amplitude plane wave with a wavelength λ of 532 nm was used. The critical distance z_c of 30.8 mm is calculated from the equation of $\frac{N\Delta x^2}{\lambda}$. No aliased fringes appear for distances above z_c .

Figure 2 illustrates the change in spatial frequency along the lateral distance. The spatial frequency along the x -axis at the center of the hologram is obtained using a commercial spectrum calculation program, in Fig. 2(a). Unlike the aliased frequencies in the real plane, both negative and positive spatial frequency components appear in the complex plane. In the complex-valued function, the position vector with negative frequencies rotates clockwise, while the position vector with positive frequencies rotates counterclockwise.

The spatial frequency exhibits a linear dependence on the lateral spatial distance. On the positive-axis side, the spatial frequency increases continuously up to the Nyquist frequency, i.e., $f_N = 1.25 \times 10^5 \text{m}^{-1}$. The position of the Nyquist frequency is estimated to be $x = 512 \mu\text{m}$ using Eq. 1. At this point, the spatial frequency changes discontinuously to the negative Nyquist value, then continues to increase toward zero. The trajectories of the position vectors in these two distinct regions are plotted in polar coordinate, as depicted in Figs. 2(b) and (c). The

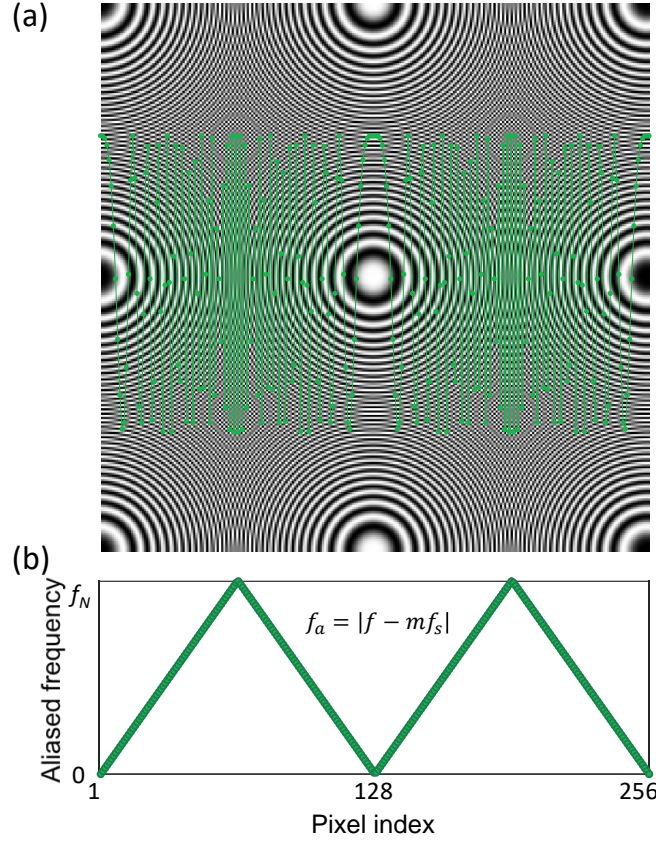


Fig. 1. Aliasing phenomenon for a point-source hologram sampled at a lower sampling rate. (a) The real-valued hologram made at a distance of a half of z_c exhibits four replica Fresnel zones. The inset graph is the 1D quadratic phase function along the lateral distance at the center. (b) Aliased frequencies for the quadratic phase function.

position vector rotates from a counterclockwise direction to a clockwise direction at the Nyquist frequency. Similarly, the negative side shows symmetrical behavior.

On the other hand, the shifted replica function is represented in a modulated form by a carrier wave function, derived from the quadratic phase term in the complex exponential function. The carrier wave is a sinusoidal wave with a period of $2\Delta x$, expressed as $e^{\frac{-i\pi x}{\Delta x}}$. This causes the replica zone to be appear as moire fringes with a low-frequency pattern. In the modulation form, the spatial frequency f is calculated as the sum of the original frequency f_o and the carrier frequency:

$$f = f_o + mf_s, \quad (4)$$

where the carrier frequency is a mutiple of the sampling frequency. Figure 2(d) draws the distribution of angular spectrum considering the modulation behavior. The spatial frequency on both sides of the x -axis increases from zero to the sampling frequency of $f_s = 2.5 \times 10^5 \text{m}^{-1}$ without any discontinuity. Likewise, all shifted replica functions can be expressed as higher spatial-frequency components corresponding to those of the original function. The analysis in the complex plane reveals that the shifted replica function represents not only aliased fringes but also higher spectrum components.

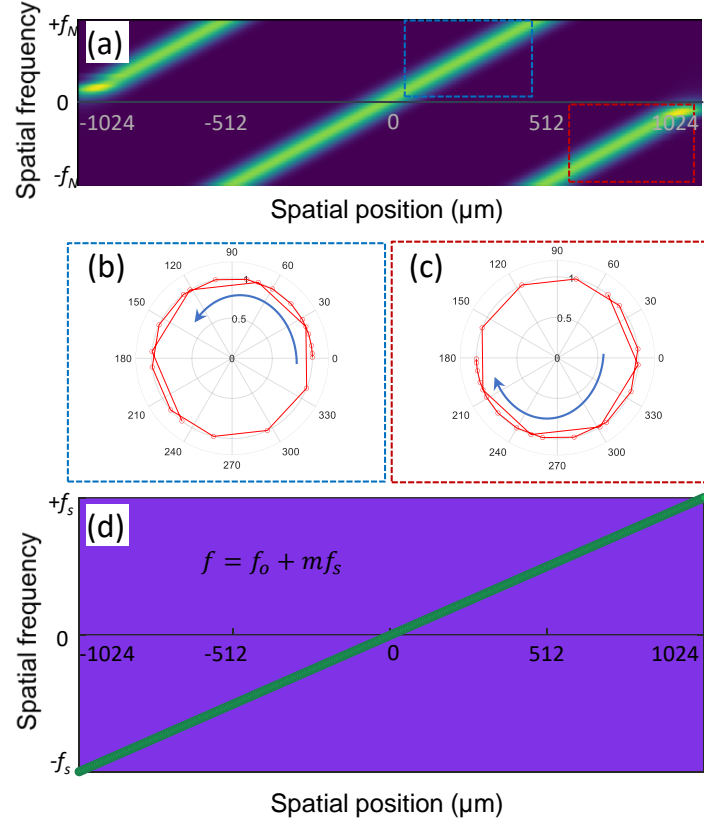


Fig. 2. Spatial frequency distribution of an undersampled point-source hologram in the complex domain. (a) Spatial frequency variation along the lateral spatial position. The trajectories of the position vectors (b) in the blue box and (c) in the red box, corresponding to those in Fig. 1(a), are plotted in polar coordinates, respectively. (d) Spatial frequency distribution after considering the modulation form by a carrier wave.

3. Imaging behaviour of undersampled hologram

Figure 3 illustrates the imaging behavior for the undersampled hologram. The diffractive wave $g(x', y')$, propagating from the hologram function $h(x, y)$, was numerically calculated by using the Rayleigh-Sommerfeld diffraction formula [1]:

$$g(x', y') = \frac{z}{i\lambda} \iint h(x, y) \frac{\exp(ikr)}{r^2} dx dy, \quad (5)$$

where an incident plane wave with a unit amplitude is assumed, and k is the wavenumber of $2\pi/\lambda$. The intensity of the diffractive waves along the lateral line at the center is displayed as a function of the propagating distance, $r = \sqrt{z^2 + (x' - x)^2 + (y' - y)^2}$. The point image is focused in the Fresnel diffraction region, and aliased replica functions generate corresponding replica images. The sampled hologram produces high-order diffraction terms that propagate in specific directions. Individual diffraction waves cannot be distinguished in the region close to the hologram.

As shown in Fig. 3(a), the point image is formed at a half of z_c , i.e., 15.4 mm, and then spreads out as it propagates further. The image resolution of $4 \mu\text{m}$ is twice as high as the hologram pixel size, and similarly, the spreading angle is double that of the diffraction angle of hologram pixel. The spreading angle is estimated to be approximately 7.6° , whereas the diffraction angle

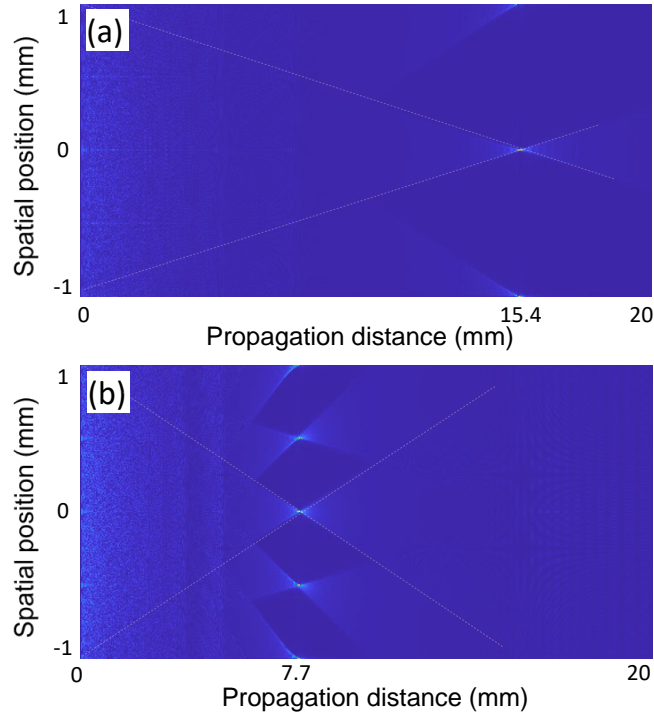


Fig. 3. Imaging behavior of an undersampled point-source hologram simulated using the Rayleigh-Sommerfeld diffraction formula. (a) Propagating waves from the hologram prepared using a point object placed at half- z_c . (b) Propagating waves from the hologram prepared using a point object placed at quarter- z_c . The intensity of the diffractive waves along the x -axis is displayed. The aspect ratio of the image is conveniently adjusted. Inset lines are included to clearly indicate the diffraction angle, θ .

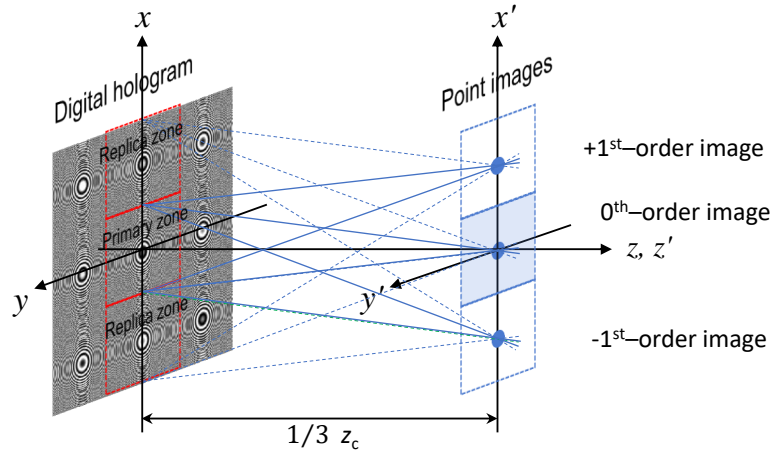


Fig. 4. Schematic diagram illustrating multiple diffractions from an undersampled hologram. Point-image reconstruction is described using a hologram made at one-third of z_c . For clarity, multiple diffractions for three Fresnel zones in the central region are drawn.

for a hologram pixel size of $8\ \mu\text{m}$ is 3.8° . The hologram made at a quarter of critical distance reconstructs the point image with a spatial resolution of $2\ \mu\text{m}$, where the spreading angle, i.e., the viewing angle increases to 15.2° , in Fig. 3(b). Both the image resolution and spreading angle increase as the synthesis distance of the digital hologram decreases. It appears that the entire aperture of the digital hologram contributes to image formation, regardless of aliasing.

Meanwhile, to clarify this property, the high-order diffractions of the replica functions are distinguished through numerical simulation. Figure 4 is the schematic diagram showing the multiple diffractions from the undersampled hologram. The reconstruction behavior from a hologram made at one-third of z_c is drawn for the sake of convenience. Replica functions generate high-order diffractions, forming replicas of the point image arranged at uniform intervals in the image plane. The Fresnel zone of replica function corresponding to the $+1^{\text{st}}$ -order image contributes to the formation of both the original image and the -1^{st} -order image. In this scenario, it becomes challenging to determine whether the enhanced spatial resolution arises from the extended high-spectrum components of the replica functions.

The angular spectrum method allows the image space to be confined within the diffraction zone of a hologram pixel, effectively eliminating interference from high-order diffractions during numerical calculations. The algorithm involves a double Fourier transform [1, 6]:

$$g(x', y') = \text{IFT} \left(\text{FT} [h(x, y)] \text{FT} \left[\exp \left[\frac{i\pi}{\lambda z} (x^2 + y^2) \right] \right] \right), \quad (6)$$

where **FT** and **IFT** indicate the Fourier transform and the inverse Fourier transform, respectively. The pixel resolutions in each space are governed by the sampling relation:

$$\Delta x' = \frac{1}{N\Delta f} = \Delta x. \quad (7)$$

The pixel values in both hologram and image planes are the same via the pixel value Δf in the intermediate Fourier plane. Only the zeroth-order region in the intermediate plane, $N\Delta f$ is utilized, thereby excluding high-frequency components beyond the diffraction limit.

Figure 5 presents the simulated diffractive waves obtained using the angular spectrum method. The high-order diffractions are removed due to an upper bound frequency of $1.25 \times 10^5 \text{m}^{-1}$, effectively functioning as a low-pass filter. The point image is formed from the primary zone which occupies half the width of the hologram aperture. The spatial resolution of the point image is $8\ \mu\text{m}$, based on Eqs. (1) and (6). The spreading angle of the propagating wave is estimated to be 3.9° .

The diffraction behavior of a two-fold upsampled hologram was investigated. The upsampling process increases the pixel resolution from 256×256 pixels at $8\ \mu\text{m}$ to 512×512 pixels at $4\ \mu\text{m}$ by simply duplicating the pixel values of the original undersampled hologram. As depicted in Fig. 5(b), each pixel in the original hologram corresponds to four identical pixels in the two-fold upsampled version. In this circumstance, while the two-fold upsampled hologram retains the replica patterns, the calculation process is performed in the two-fold enhanced Fourier space, based on Eq. (6). There is no confinement by the upper bound frequency.

Previously, we reported that this type of upsampling process effectively suppresses high-order diffractive waves [13]. The two-fold upsampling process restrains the $\pm 1^{\text{st}}$ -order images. The propagating behavior in Fig. 5(c) demonstrates an absence of interference from multiple diffractions caused by replica functions. Irrespective of high-order terms by neighbouring replica functions, the central point image is formed through the entire region of the digital hologram. The diffracted wave converges at an angle of 7.2° before focusing on the point image, achieving a spatial resolution of $4\ \mu\text{m}$.

This behavior clearly shows that the spatial frequency continuously increases across the shifted replica functions. Therefore, even the maximum spatial frequency in the undersampled hologram

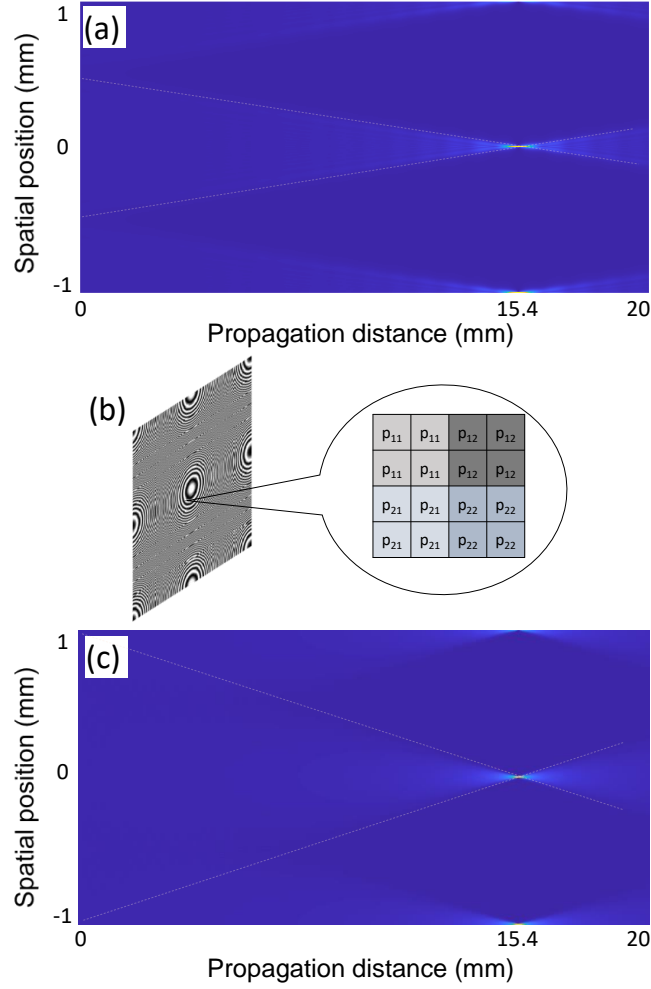


Fig. 5. Simulated propagating waves using the angular spectrum method. (a) High-order diffractions are eliminated and the point image is formed from the primary zone. (b) The upsampling process is performed by duplicating the pixel values of the original undersampled hologram. (c) The diffraction behavior of the two-fold upsampled hologram is illustrated.

is defined by the entire aperture of the hologram in Eq. (1). Numerical simulation well matches with the theoretical description. The spatial resolution and viewing angle of the restored image are not fixed from the diffraction angle by a hologram pixel. It is apparent that these values vary depending on the focal distance in a digital hologram with finite space-bandwidth, in Fig. 6. Previously, it was reported that the viewing angle changes according to this relationship, as demonstrated in optical experiments [13].

4. Discussions

The imaging performance depends on the space-bandwidth product of the digital hologram. A digitized device with a large space-bandwidth product is essential for reconstructing high-resolution images at a large scale. Since the hologram undersampled by a low-resolution pixel includes components of higher spatial frequencies, a high-resolution and large-scale image can

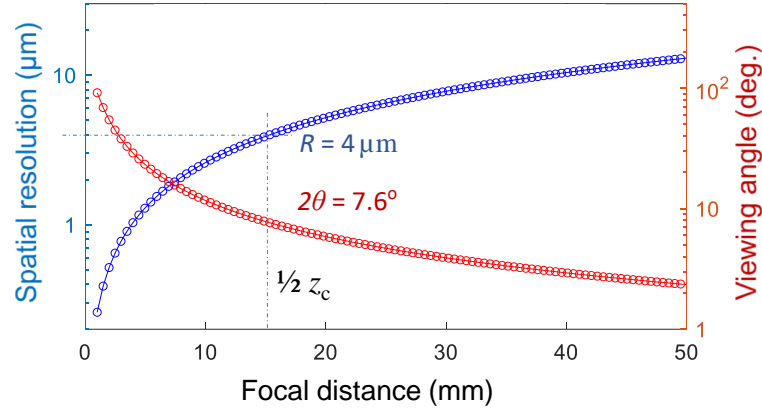


Fig. 6. Spatial resolution and viewing angle of the restored image as a function of focal distance. The inset line indicates the values for the focused image at a distance of a half of z_c .

be obtained using a digitized device with finite bandwidth, provided that methods are developed to eliminate additive noise, such as replica patterns and high-order diffractions.

In holographic displays, the limited viewing angle remains a significant bottleneck for commercializing three-dimensional displays [16–19]. A 3D image is reconstructed by illuminating the pixelated modulator loading the digital hologram with a coherent plane wave. Commercial modulators can typically achieve only a few degrees of viewing angle at best. However, by leveraging the angular spectrum distribution properties of undersampled holograms, even commercial modulators can achieve a sufficiently large viewing angle. Previously, we explored a method to extend the viewing angle beyond the diffraction limit in a commercial spatial light modulator. This study further clarifies the proposed process, which primarily consists of two steps: First, an optimization algorithm is developed to suppress the formation of replica patterns in the undersampled hologram [14]. Second, an upsampling process is applied to eliminate high-order diffractions. This is achieved by attaching a fine-definition grid to the pixelated modulator [13].

5. Conclusions

A mathematical description of the angular spectrum distribution demonstrates that an under-sampled hologram at a lower sampling rate can reconstruct an image with the same spatial resolution and angular field of view as a properly sampled hologram. The spatial frequencies are found to be continuously distributed across the aliased replica functions. Moreover, the undersampled replica functions differ from the meaningless noise typically associated with conventional aliasing. Instead, they generate high-order diffractive waves that form replica images in the image plane. When these replica terms are effectively removed through suitable external operations, high-performance imaging can be achieved, surpassing the inherent space-bandwidth limitations of a digital hologram. One practical example of this concept addresses the issue of limited viewing angles in holographic displays. This technology provides an alternative approach to overcome the finite space-bandwidth constraints of digital holograms, paving the way for enhanced imaging performance.

Funding. This work was partially supported by Institute for Information & Communications Technology Promotion (IITP) grant funded by the Korea government (MSIP) (2021-0-00745)

Disclosures. The authors declare no conflicts of interest.

References

1. J. W. Goodman, *Introduction to Fourier Optics* (McGraw-Hill, 1996).
2. A. W. Lohmann, R. G. Dorsch, D. Mendlovic, Z. Zalevsky, and C. Ferreira, "Space-bandwidth product of optical signals and systems," *J. Opt. Soc. Am. A* **13**, 470-473 (1996).
3. P. Picart and J. Leval, "General theoretical formulation of image formation in digital Fresnel holography," *J. Opt. Soc. Am. A* **25**(7), 1744-1761 (2008).
4. D. P. Kelly, B. M. Hennelly, N. Pandey, T. J. Naughton, and W. T. Rhodes, "Resolution limits in practical digital holographic systems," *Opt. Eng.* **48**(9), 95801 (2009).
5. T. Latychevskaia and H.-W. Fink, "Inverted Gabor holography principle for tailoring arbitrary shaped three-dimensional beams," *Sci. Rep.* **6**, 26312 (2016).
6. B. G. Chae, "Analysis on angular field of view of holographic image dependent on hologram numerical aperture in holographic display," *Opt. Eng.* **59**(3), 035103 (2020).
7. T. M. Kreis, "Frequency analysis of digital holography," *Opt. Eng.* **41**(4), 771-778 (2002).
8. L. Onural, "Sampling of the diffraction field," *Appl. Opt.* **39**(32), 5929-5935 (2000).
9. A. Stern and B. Javidi, "Analysis of practical sampling and reconstruction from Fresnel fields," *Opt. Eng.* **43**(1), 239-250 (2004).
10. B. G. Chae, "Analysis on image recovery for on-axis digital Fresnel hologram with aliased fringe generated from self-similarity of point spread function," *Opt. Commun.* **466**, 125609 (2020).
11. A. V. Oppenheim, A. S. Willsky, and S. H. Nawab, *Signals and Systems* (Prentice-Hall, 2010).
12. L. Onural, "Some mathematical properties of the uniformly sampled quadratic phase function and associated issues in Fresnel diffraction simulations," *Opt. Eng.* **43**(11), 2557-2563 (2004).
13. B. G. Chae, "Wide viewing-angle holographic display based on enhanced-NA Fresnel hologram," *Opt. Express* **29**(23), 38221-38236 (2021).
14. B. G. Chae, "Viewing-angle expansion in holographic displays implemented with a modulator having finite space-bandwidth," *Opt. Express* **31**(23), 37900-37910 (2023).
15. B. G. Chae, "Spatial resolution enhancement in holographic imaging via angular spectrum expansion," *Opt. Continuum* **3**(3), 263-277 (2024).
16. T. Kozacki, M. Kujawińska, G. Finke, B. Hennelly, and N. Pandey, "Extended viewing angle holographic display system with tilted SLMs in a circular configuration," *Appl. Opt.* **51**(11), 1771-1780 (2012).
17. K. Yamamoto, Y. Ichihashi, T. Senoh, R. Oi, and T. Kurita, "3D objects enlargement technique using an optical system and multiple SLMs for electronic holography," *Opt. Express* **20**(19), 21137-21144 (2012).
18. Y. Takaki and S. Uchida, "Table screen 360-degree three-dimensional display using a small array of high-speed projectors," *Opt. Express* **20**(8), 8848-8861 (2012).
19. M. Gopakumar, J. Kim, S. Choi, Y. Peng, and G. Wetzstein, "Unfiltered holography: optimizing high diffraction orders without optical filtering for compact holographic displays," *Opt. Lett.* **46**(23), 5822-5825 (2021).